# Hollandite-type Potassium Titanium Oxide with Exceptionally Stable Cycling Performance as a New Cathode Material for Potassium-ion Batteries

Jae Hyeon Jo[a,b,z], Hee Jae Kim[a,z], Najma Yaqoob[c], Kyuwook Ihm[d], Oliver Guillon[c], Kee-Sun Sohn[a], Naesung Lee[a], Payam Kaghazchi[c,e,*], Seung-Taek Myung[a,*]

[a]*Hybrid Materials Research Center, Department of Nanotechnology and Advanced Materials Engineering & Sejong Battery Institute, Sejong University, 98 Gunja-dong, Gwangjin-gu, Seoul 05006, South Korea*

[b]*Korea Electronic Power Research Institute(KEPRI), Daejeon, 34056, South Korea*

[c]*Forschungszentrum Jülich GmbH, Institute of Energy and Climate Research, Materials Synthesis and Processing (IEK-1), Jülich 52425, Germany*

[d]*Pohang Accelerator Laboratory, 80 Jigokro-127-beongil, Nam-gu, Pohang, Gyeongbuk 37673, Korea*

[e]*MESA+ Institute for Nanotechnology, University of Twente, 7500 AE Enschede, the Netherlands*

[z]*These authors contributed equally to this work.*

*Corresponding Author

E-mail: p.kaghazchi@fz-juelich.de (P. Kaghazchi)

E-mail: smyung@sejong.ac.kr (S. Myung)

**Abstract**

For the first time, we introduce hollandite-type $K_{0.17}TiO_2$, in which potassium ions are located at the center of a (2 × 2) tunnel structure, as a potential cathode material for potassium-ion batteries. Density functional theory calculation predicts the possibility of $K^+$ insertion into the hollandite-type tunnel structure *via* a single-phase reaction. *Operando* X-ray diffraction and X-ray absorption spectroscopy analyses verify that potassium ions are de-/intercalated from/into the crystal structure of $K_{0.17}TiO_2$, accompanied by a $Ti^{4+}/Ti^{3+}$ redox reaction. The single-phase reaction is sustainable for long-term cycling, with exceptionally high operation voltage over 2.5 V. The hollandite-type $K_{0.17}TiO_2$ cathode delivers a reversible capacity of 60 mAh $g^{-1}$ at 5 C (1.55 A $g^{-1}$), with excellent capacity retention of over 98 % of the initial capacity for 1000 cycles. This performance is related to the single-phase reaction with good structural stability. This work presents a facile approach that enables the use of a cathode with stable tunnel structure for potassium-ion batteries.

**Keywords**: Hollandite-type; $Ti^{4+}/Ti^{3+}$ redox; Cathode; Potassium: Battery.

## 1. Introduction

Lithium-ion batteries (LIBs) have received significant attention as power sources for portable electronics and electric vehicles (EVs) owing to their high energy densities, with a recent focus on increasing the energy density of LIBs to satisfy demands from markets. However, the widespread use of LIBs for large-scale applications is hindered by the recent surge in the price of lithium. Many efforts have thus been devoted to searching for LIB alternatives, namely, the use of sodium or potassium ions as charge carriers despite their ionic radii ($Na^+$: 1.02 Å and $K^+$: 1.38 Å) being larger than that of lithium ($Li^+$: 0.76 Å). Notably, there is a price advantage when using earth-abundant sodium and potassium ions as charge carriers in sodium-ion batteries (SIBs) and potassium-ion batteries (KIBs), respectively. The standard electrode potential of potassium metal ($K^+$/K: −2.93 V vs. standard hydrogen electrode (SHE)) is comparable to that of lithium metal ($Li^+$/Li: −3.04 V vs. SHE). In addition, the potassium ion possesses weaker Lewis acidity and a smaller Stokes radius compared with those of lithium and sodium ions, implying reasonable ionic conductivity of $K^+$ in the electrolyte. To date, various potassium storage materials, such as layered transition-metal oxides [1–9], polyanions [10–14], Prussian blue analogues [15–21], and organic compounds [22, 23], have been evaluated as cathode materials for KIBs. Among these materials, the layered P2- [1–3], P'2- [4], and P3-type $K_xTMO_2$ [1,5,9] ($x \leq 0.8$, TM = transition metal) electrodes have exhibited gradual capacity fading upon cycling due to repetitive extraction/insertion of the large $K^+$ ions into/out of the crystal structure. Among them, Luo *et. al.* applied $Mg^{2+}$ substitution into transition metal layers of P3 type layered $K_{0.5}MnO_2$, effectively suppressing Jahn-Teller distortion and phase transition during charge/discharge [9]. Polyanion compounds, such as $K_3V_2(PO_4)_3$ [12], $KVOPO_4$ [13], $KVPO_4F$ [13], and $KVP_2O_7$ [14], have been reported as 4 V-class cathode materials, which is associated with the inductive effect of the covalent P–O bond in the compounds. These compounds exhibit reasonable capacity (~100 mAh $g^{-1}$), similar to that of layered materials (~110–120 mAh $g^{-1}$). However, the main electroactivity is observed in the presence of vanadium, which is as expensive as Ni and toxic, such that identifying appropriate cathode materials with rigid structures is an important step for further development of KIBs.

Titanium dioxide ($TiO_2$) is abundant and inexpensive and has polymorphs of anatase (space group: $I4_1/amd$), rutile ($P4_2/mnm$), brookite ($Pbca$), bronze ($C2/m$), ramsdellite ($Pbnm$), hollandite ($I4/m$), columbite ($Pbcn$), and baddeleyite ($P2_1/c$). Among these structures, hollandite-type $TiO_2$ has large (2 × 2) tunnels, which consist of single or multiple chains of edge-sharing $TiO_6$ octahedra that share corners with other chains to constitute a structure with tunnels. Interestingly, potassium ions ($K^+$) can be placed into the (2 × 2) tunnel along the *c*-axis in the range of $0.125 \leq y \leq 0.25$ in $K_yTiO_2$ [24, 25]. In earlier works, it was reported that the residual $K^+$ ions could not be electrochemically extracted and impede the diffusion of $Li^+$ ions in the tunnels during discharge and charge processes in LIBs [26]. Acid-leaching using $HCl/HNO_3$ appeared to be effective for the removal of the residual $K^+$ ions from $K_{0.13}TiO_2$ to $K_{0.008}TiO_2$ [27, 28]. $Li^+$ insertion was available into the depotassiated $K_{0.008}TiO_2$ in Li cells, resulting in the first discharge capacity of approximately 158 mAh $g^{-1}$, although the structural changes occurring during the lithiation process were not clear. Moreover, achievement of 'in-depth' insights for $K^+$ ion storage electrochemistry is essential, in order to develop highly qualified $K^+$ ion storage materials [29–32].

For tunnel-type $K_yTiO_2$ ($0.125 \leq y \leq 0.25$), efforts to insert $K^+$ into the (2 × 2) tunnel have not yet been made in KIBs, motivating us to examine the capability of $K_{0.17}TiO_2$ as a $K^+$ intercalation material. We first investigated the feasibility of $K_{0.17}TiO_2$ as a cathode material using density functional theory (DFT) calculation, which predicted intercalation of $K^+$ into the (2 × 2) tunnel structure and produced a voltage profile that was fairly consistent with the experimentally observed voltage profile. Theoretical investigation demonstrated that the (2 × 2) tunnel structure underwent a single-phase reaction accompanied by the $Ti^{4+/3+}$ redox pair during $K^+$ insertion. The $K_{0.17}TiO_2$ cathode delivered a specific capacity of 79 mAh $g^{-1}$ at 0.05 C (15.5 mA $g^{-1}$) with capacity retention of 83% for 300 cycles and 60 mAh $g^{-1}$ at 5 C (1.55 A $g^{-1}$) with excellent capacity retention of 98% for 1000 cycles. An *operando* X-ray diffraction (*o*-XRD) study verified the prediction that $K^+$ ions were inserted into the tunnel during potassiation and *vice versa* on depotassiation *via* a single-phase reaction. It is also noteworthy that the monotonous phase reaction was retained throughout the cycling, as confirmed by *o*-XRD after 1000 cycles. It is likely that such structural stability is responsible for the outstanding electrode performance, although the large $K^+$ ions were repetitively introduced into the tunnel structure. We herein report on the physical and electrochemical characteristics of $K_{0.17}TiO_2$ as a cathode material for KIBs.

## 2. Experimental

### 2.1. Material preparation

$K_{0.17}TiO_2$ was synthesized through a conventional ceramic process; in detail, $K_2CO_3$ and $TiO_2$ were uniformly mixed using high-energy ball milling (As One, PM-001, Japan) at 350 rpm for 3 h. This powder mixture was calcined at 1000 °C for 10 h under an $Ar/H_2$ (4 % $H_2$ in Ar gas) atmosphere and subsequently cooled to room temperature.

### 2.2. Characterization

The structural properties of the as-synthesized $K_{0.17}TiO_2$ were analyzed by X-ray diffraction (XRD; X'Pert, PANalytical). The XRD measurements were performed in the range of 10°–80° (2θ) with a step size of 0.03°, and then, the resulting XRD data were refined using the FullProf Rietveld program. The chemical compositions of $K_{0.17}TiO_2$ were investigated using inductively coupled plasma–atomic emission spectroscopy (ICP-AES; OPTIMA 8300, Perkin-Elmer). Field-emission scanning electron microscopy (FE-SEM, JSM 6400, JEOL) and high-resolution transmission electron microscopy (HR-TEM; JEM-3010, JEOL) with energy-dispersive X-ray spectroscopy (EDS; 7200-H, HORIBA) were employed to identify the particle morphologies and element analysis. Furthermore, the phase-transition mechanism of $K_{0.17}TiO_2$ was investigated using *operando* XRD (*o*-XRD, X'Pert, PANalytical) and *ex-situ* X-ray absorption spectroscopy (XAS) performed at beamlines 8C and 4D of the Pohang Accelerator Laboratory (PAL), Pohang, South Korea.

**2.3. Electrochemical measurements**

The cathode was fabricated by blending the produced active material, conducting materials (Super-P:Denka black by 1:1 in weight), and polyvinylidene fluoride (PVdF) binder (80:10:10 by weight) in *N*-methyl-2-pyrrolidone (NMP) to form a slurry. The slurry was casted on Al foil using a doctor blade and then dried at 110 °C in a vacuum oven. The prepared electrode was assembled in R2032 coin cells with potassium metal as the anode in presence of 0.5 M KFSI (potassium bis(fluorosulfonyl)imide) in ethylene carbonate (EC)–dimethyl carbonate (DEC) (1:1 by volume %) solvents as the electrolyte in an Ar-filled glove box. The cells were tested in the operating range between 1.0 and 4.2 V at designated rates (0.05 C: 15.5 mA $g^{-1}$).

**2.4. Computation**

Spin-polarized DFT calculations were performed using the projector augmented wave (PAW) [33] potential method implemented in the Vienna *Ab Initio* Simulation Package (VASP) code [34]. The generalized gradient approximation (GGA) within the scheme of Perdew–Burke–Ernzerhof (PBE) [35] was selected as the exchange-correlation functional. To perform the Coulomb energy analysis and DFT calculation, we modeled $K_yTiO_2$ ($y$ = 0.00, 0.021, 0.042, 0.083, 0.125, 0.167, 0.208, and 0.25) structures with a 1 × 1 × 6 supercell (for example, $K_{0.25}TiO_2$ modeled by $K_{12}Ti_{48}O_{96}$). A $k$-point mesh of 2 × 2 × 1 and an energy cut off of 500 eV were applied. Electronic and force convergence criteria of $10^{-4}$ eV and $10^{-3}$ eV Å$^{-1}$, respectively, were considered for DFT calculations. Total Coulomb energy ($E_c$) calculation on the possible configurations were performed using the so-called *supercell* code [36]. Atomistic structures were visualized with the VESTA program [37].

## 3. Results and discussion

**Fig. S1** presents XRD patterns of the as-prepared $K_yTiO_2$ powders with different K:Ti ratios. It is considered that the single-phase formation range is quite narrow, because slight variation in K:Ti ratio resulted in formation of impurities. Accordingly, the $K_yTiO_2$ prepared with the 1:5 molar ratio was crystallized into the single phase hollandite structure. The corresponding chemical composition was determined to be $K_{0.17}TiO_2$ by ICP-AES analysis, as slight amount of K was evaporated during the calcination at high temperature. The resulting crystal structure was investigated through Rietveld refinement of the XRD data assuming a tetragonal structure with $I4/m$ space group, as shown in **Fig. 1a**. The observed XRD pattern of the as-synthesized $K_{0.17}TiO_2$ coincided with the calculated one, with lattice parameters of $a$-axis: 10.176(2) Å and $c$-axis:

2.965(2) Å (**Table S1**). The crystal structure is visualized in **Fig. 1b**, based on the data obtained from the Rietveld refinement for $K_{0.17}TiO_2$ (**Table S1**). Based on the Rietveld refinement of the XRD data (**Table S1**), we present the corresponding crystal structure with bond valence sum (BVS) energy maps of $K_{0.17}TiO_2$ (**Fig. 1b**). $K_{0.17}TiO_2$ has a (1 × 1) and (2 × 2) tunnel structure with $K^+$ ions in the center of the (2 × 2) tunnel along the *c*-axis. The BVS energy map elucidates the possibility of $K^+$ intercalation into the $K_{0.17}TiO_2$ tunnel structure. As a result, $K^+$ is accommodated at the center site with Wyckoff positions and atomic coordinates ($x$, $y$, $z$) of 2*b* (0, 0, 0.5) in the (2 × 2)-type tunnel (denoted by a yellow dorsal surface like water flow) using multiple 1D potassium diffusion paths along the *c*-axis direction of the tunnel. However, $K^+$ ions cannot be occupied in the (1 × 1) type tunnel, presumably due to the large size of the $K^+$ ions. DFT calculation by Koyama *et al.* shows that the formation energy of transition metal vacancy $V_M$ in transition-metal oxides (i.e. $LiCoO_2$, $LiNiO_2$, $LiMnO_2$, and $Li(Li_{1/3}Mn_{2/3})O_2$) is so high that the concentration of $V_M$ is lower than $10^{-5}$ per formula unit [38]. The concentration of $V_{Ti}$ is expected to be also much lower than that of Wyckoff sites in $TiO_2$ at room temperature. Hence, the incorporation of K into point defects, most likely, would not play any role in controlling the charge/discharge process. The hollandite-type $K_{0.17}TiO_2$ is crystallized with an average length ranging from 0.5 to 2 μm, as shown in **Fig. 1c and d**. The EDS mapping images confirm the uniform distribution of K, Ti, and O elements in the particle. Furthermore, the HR-TEM image shows well-developed layers, in which the interlayer distance matches with the *d*-spacing of 5.09 Å for the (200) plane (**Fig. 1e**), showing the related (220), (110), and (200) planes in the selected-area electron diffraction (SAED) pattern along the [100] zone axis.

Using electrostatic analysis (see Supplementary Information) and DFT calculation, we computed the (lowest total energy) atomistic structure, formation energy, and voltage profile of the K-inserted $TiO_2$ compound, namely $K_yTiO_2$ (**Fig. 2**) [39]. The formation energy $E_F$ of $K_yTiO_2$ from the two end compounds, i.e., the fully potassiated $K_{0.25}TiO_2$ and depotassiated $TiO_2$, were obtained using their corresponding total energies $E$ (**Fig. 2a**):

$$E_F = E(K_{0.25x}TiO_2) - [xE(K_{0.25}TiO_2) + (1-x)E(TiO_2)],\ y = 0.25x \qquad (1).$$

The voltage curve (**Fig. 2b**) was then calculated using the total energies of the determined adjacent most favorable K-inserted $TiO_2$ compounds, namely $E(K_{y_i}TiO_2)$ and $E(K_{y_j}TiO_2)$, from the formation energy plot:

$$V(y_i, y_j) = -\frac{E(K_{y_j}TiO_2) - E(K_{y_i}TiO_2) - (y_j - y_i)E(K)}{(y_j - y_i)} \qquad (2).$$

Here, $E$(K) is the energy per formula unit of bulk metal K. The formation energy was observed to change almost linearly between $y$ = 0.021 and $y$ = 0.125, and the voltage did not change much with $y$ in this range. This result indicates that at the low K concentrations, the K–K interaction is very weak. This is because there is enough space for $K^+$ ions to occupy free K sites with the largest possible separations from each other (**Fig. 2c**). The result is consistent with the BVS energy map result presented in **Fig. 1b**. The shortest K–K distance between $K^+$ ions occupying the same channel and neighbor channels for $0.021 \leq y \leq 0.125$ are $d_{K–K} \geq 5.96$ Å and $d_{K–K} \geq 7.35$ Å, respectively. However, a strong K–K repulsion occurs for K concentrations larger than y=0.125 as $K^+$ ions must occupy free K sites between already occupied K sites. The $d_{K–K}$ distances in $K_yTiO_2$ with $0.125 \leq y \leq 0.250$ is ≥ 3.00 Å. This leads to a gradual decrease in voltage for $0.125 \leq y$. The end points of the computed voltage profile reasonably agree with the observed voltage curve (**Fig. 3a**). The calculated voltage has a voltage plateau at approximately 3 V in the range of $y$ = 0–0.11 in $K_yTiO_2$, which is exceptionally high considering the $Ti^{4+}/Ti^{3+}$ redox potential that usually emerges at 1.6–1.8 V in $Li_4Ti_5O_{12}$ and $TiO_2$ in Li cells, of which the potential can be converted to

1.5–1.7 V versus $K^+/K$ based on the standard electrode potential. Even for the similar hollandite $Li_xTiO_2$, the reported operation voltage by $Ti^{4+}/Ti^{3+}$ was approximately 2.3 V, which is far lower than that observed in the present $K_yTiO_2$, ~3 V [27]. The only difference between hollandite $K_yTiO_2$ and $Li_yTiO_2$ is the coordination of K (binding with 8 oxygens) and Li (binding with four oxygens) in the open tunnels. It is hypothesized that such a difference in environment for the alkali ions results in the exceptionally high operation voltage for $y$ = 0–0.11 in $K_yTiO_2$. To verify this hypothesis, we computed the voltage for $TiO_2$ with a low concentration of Li, namely $Li_{0.021}TiO_2$, and observed a value of 2.29 V for Li at a four-coordinated site (**Fig. 2d**).

The as-synthesized hollandite-type $K_{0.17}TiO_2$ electrode was tested in the range of 1.0–4.2 V at a rate of 0.05C (15.5 mA $g^{-1}$) in K cells. Regarding the calculated theoretical capacity of $K_{0.17}TiO_2$ of 335 mAh (g-oxide)$^{-1}$ (based on one-electron reaction of $Ti^{4+}/Ti^{3+}$ redox with 1 mole of $K^+$ insertion in $TiO_2$ framework), the obtained charge and discharge capacities of the $K_{0.17}TiO_2$ electrode were 37 and 79 mAh $g^{-1}$, respectively, at the first cycle (**Fig. 3a**). As predicted in the DFT calculation in **Fig. 2a and b**, the depotassiation resulted in a steep rise of the operation voltage to 3.2 V, which stems from $K^+$/vacancy ordering in the tunnel structure, after which the voltage increased gradually to 4.2 V. Such emergence of a voltage plateau at high voltage is attributed to the presence of strong binding energy generated by the K–O bond in the tunnel structure. The insufficient delivery of capacity in the range of $y$ = 0–0.06 in $K_yTiO_2$ (~21 mAh $g^{-1}$) is most likely due to the difficulty of $K^+$ extraction from the $K_yTiO_2$ tunnel in the experiment, which requires more energy by raising the charge cutoff voltage to fully extract $K^+$ ions. There was an emergence of a voltage plateau at approximately 3.1 V on potassiation, and the ordering was again evident in the range of 2.6–2.9 V. The reversibility is observed in the $d$Q/$d$V profile for the second cycle (**Fig. 3b**). The voltage profile became sloppy as potassiation further progressed, accompanied by an additional plateau below 1.5 V, compared with the second discharge capacity of approximately 70 mAh $g^{-1}$ (**Fig. 3a**). The capacity difference (~9 mAh $g^{-1}$) between the first and second discharge is attributed to the formation of a solid-electrolytic interphase (SEI) on the carbons used as the conducting agent below 1.5 V, as the conducting agents possessed a large capacity below 1.5 V (**Fig. S2**), in addition to reductive decomposition of the electrolyte. ICP-AES analysis indicated a slight increase in the K content when discharged to 1.5 V (0.241 mol K per formula unit) and 1 V (0.273 mol), of which the value did not change after the second discharge to 1 V (0.273 mol) (**Table S2**). This finding agrees with our assumption that the additional 0.027 mol K (~9 mAh $g^{-1}$) contributed to the reaction with the conducting agent at the first discharge. Except for the first cycle, there were no differences in the voltage profiles even after 300 cycles, showing 94% retention of the second discharge capacity (**Fig. 3c**). The high voltage plateau at 3 V and the $K^+$/vacancy ordering in the structure were still visible at the 300th cycle.

Fast and reversible migration of $K^+$ ions into/out of the tunnel structure was also confirmed up to 5C (1.55 A $g^{-1}$), resulting in a discharge capacity of approximately 60 mAh $g^{-1}$, which is 87% of the capacity at 0.05C (**Fig. 3d and e**). Because of the activity at 5C (1.55 A $g^{-1}$), the $K_{0.17}TiO_2$//K cell was further monitored for 1000 cycles (**Fig. 4**). The $K_{0.17}TiO_2$ electrode delivered a capacity of approximately 58.7 mAh $g^{-1}$ at the 1000th cycle, thus retaining over 98% of the initial capacity for 1000 cycles with a Coulombic efficiency > 99.9%, as shown in **Fig. 4a and b**. It is evident that the capacity of $K_{0.17}TiO_2$ is smaller than that of layered cathode materials at low rates [3–5, 7]; however, it is noteworthy that the tunnel structure enables stable long-term delivery of capacity at high rates as well as high operation voltage over 2.5 V (**Fig. 4c**). Furthermore, we added a sacrificial salt, $K_2C_4O_4$ (9 *wt*. %) to compensate the deficient $K^+$ on the first charge (**Fig. S3**) [40]. Accordingly, a long voltage plateau was observed over 4 V, which is associated with $K^+$ release by decomposition of $K_2C_4O_4$ salt, resulting in the first Coulombic efficiency of 96.4 %.

*Operando* XRD (*o*-XRD) analysis was performed to understand the structural evolution during de/potassiation of $K_{0.17}TiO_2$ in K cells (**Fig. 5**). During the depotassiation (charge) to 4.2 V ($y$ = 0.06 in $K_yTiO_2$), the (310), (040), and (420) planes of $K_{0.17}TiO_2$ slightly shifted toward higher angle (2θ), whereas the (121) and (031) planes shifted to lower angle (2θ). This variation is associated with $K^+$ being extracted from the (2 × 2) tunnel structure, leading to contraction of the tunnel size that results in a decrease of the *a*-axis parameter (**Fig. 5a and b**). However, the length of the tunnel in the depth direction was expanded, resulting in the increase of the *c*-axis parameter. The reduction in the *a*-axis lattice parameters on charge is related to the reduction of the Ti–O1 and Ti–O2 bonds, whereas the lengths of the Ti–O1 and Ti–O2 bonds increase during the insertion of $K^+$ [28]. The linear variation in the lattice parameters is typically observed when a single-phase reaction prevails in the structure. The volume variation was negligible (below 0.1%), namely 306.9 $Å^3$ for $K_{0.06}TiO_2$ and 307.3 $Å^3$ for $K_{0.27}TiO_2$. A similar tendency was observed for hollandite-type $K_xTiO_2$ with different K content in the tunnel space [41]. Unlike other layered compounds [3, 5, 7] or phosphate-based materials [13, 42] that exhibit multiple phase transitions, the electrochemical reaction progressed *via* a reversible single-phase reaction for $K_{0.17}TiO_2$. For the fresh $K_{0.17}TiO_2$ electrode, the average oxidation state of Ti was lower than that of the reference $TiO_2$ (4+) (**Fig. 5c**). After the depotassiation to 4.2 V, the Ti K-edge spectrum was slightly shifted toward higher photon energy, implying oxidation of Ti toward 4+. After the potassiation to 1 V, the Ti K-edge XANES spectrum moved to lower energy than that of the fresh state, and a linear increase in the a-axis parameters was observed. From these findings, it is evident that $K^+$ ions were intercalated into the (2 × 2) tunnel structure during potassiation to $K_{0.27}TiO_2$. O K-edge XANES spectra also show that there were no changes in the $e_g$ (533.2 eV) orbital, indicating the related reaction is solely associated with the $Ti^{4+}/Ti^{3+}$ redox pair for $K_{0.17}TiO_2$ (**Fig. 5d**). In addition, an oxygen-redox reaction is excluded for the activity that appeared at high voltage because the K–O–A (A: mobile ion) configuration in $K_y[A_zTM_{1-z}]O_2$ ($z < 1/3$, TM: Ti) is not observed in the present $K_{0.17}TiO_2$. This finding validates the idea that the unexpected high voltage plateau over 3 V is attributed to the $Ti^{4+}/Ti^{3+}$ redox pair, of which a strong binding energy of K–O is dominant when the $K^+$ concentration in $K_yTiO_2$ is deficient in the tunnel structure. Therefore, it is suggested that the present hollandite type (2 × 2) tunnel structure is sufficiently tolerable to allow the large $K^+$ ions in $K_yTiO_2$, accompanied by the single-phase reaction *via* the $Ti^{4+}/Ti^{3+}$ redox couple.

The structural stability of hollandite-type $K_{0.17}TiO_2$ was further identified after 1000 cycles *via* Rietveld refinement of XRD data and *o*-XRD and HR-TEM analyses (**Fig. 6**). As shown in **Fig. 6a**, the resulting structure after the long-term cycling test did not change compared with that of the fresh material. Note that the post-cycled electrode retained its original high crystallinity without impurities, and the variation of the lattice parameters relative to those of the fresh material was negligible: $\Delta a$ = 0.0047 Å, $\Delta c$ = 0.0027 Å, and $\Delta vol$ = 0.001 Å$^3$. Although the particle shape of $K_{0.17}TiO_2$ was slightly altered after 1000 cycles, K, Ti, and O elements were detected, as shown in the EDS mappings (**Fig. 6b**). The HR-TEM image (**Fig. 6c**) indicates a similar *d*-spacing for the (310) plane, estimated to be 3.32 Å, as that of the fresh state. The post-cycled $K_{0.17}TiO_2$ electrode after 1000 cycles was re-graded at 0.05C (15.5 mA $g^{-1}$) and examined using *o*-XRD to confirm the phase transition. The *o*-XRD data still present the single-phase reaction even after 1000 cycles (**Fig. 6d**), indicating that the hollandite (2 × 2) tunnel structure is sufficiently stable to accommodate the large $K^+$ ions for extensive cycling. These findings suggest the potential of hollandite-type $K_{0.17}TiO_2$ as a long-term sustainable cathode material for KIBs (**Fig. 6e**). We compared the present with previously reported tunnel type $K_yTiO_2$ with $Li^+$ or $Na^+$ as charge carriers, respectively (**Table 1**). As mentioned in our DFT calculation, $K^+$ insertion cannot exceed y = 0.25 in $K_yTiO_2$; otherwise, the tunnel is collapsed. Also, the present work is the only result that succeeded to insert $K^+$ into the $K_yTiO_2$ hollandite structural frame. Earlier works on $K_yTiO_2$ (y = 0.08 [25], 0.095 [28], and 0.13 [28]) demonstrated Li storage ability in the same structure, although the present $K_{0.17}TiO_2$ exhibited better electrode performances even for intercalation of the large $K^+$ ions that enables 98 % retention of capacity after 1000 cycles at 1.55 A $g^{-1}$.

## Conclusions

For the first time, we introduced hollandite-type $K_{0.17}TiO_2$, in which potassium ions are located at the center of a (2 × 2) tunnel structure, as a cathode material for KIBs. The potassium ions were de-/intercalated from/into the crystal structure of $K_{0.17}TiO_2$ accompanying a $Ti^{4+}/Ti^{3+}$ redox couple during the charge and discharge process, and the unexpected $Ti^{4+}/Ti^{3+}$ redox activated over 3 V was attributed to the strong binding energy of the K–O bond in the tunnel structure. The hollandite-type $K_{0.17}TiO_2$ cathode delivered a reversible capacity of 79 mAh $g^{-1}$ at 0.05C and exhibited excellent capacity retention (over 98% of the initial capacity) for 1000 cycles at 5C. This performance is related to the single-phase reaction with structural stability showing below 1% variation during de/potassiation. Our findings are expected to be beneficial for the development of cathode materials for forthcoming KIBs.

## References

[1] Y. Hirnonaka, K. Kubota, S. Komaba, P2- and P3- $K_xCoO_2$ as an electrochemical potassium intercalation host, Chem. Commun. 53 (2017) 3693–3696. https://doi.org/10.1039/C7CC00806F.

[2] H. Kim, J. C. Kim, S.-H. Bo, T. Shi, D.-H. Kwon, G. Ceder, K-ion batteries based on a P2-type $K_{0.6}CoO_2$ cathode, Adv. Energy Mater. 17 (2017) 1700098. https://doi.org/10.1002/aenm.201700098.

[3] K. Sada, B. Senthilkumar, P. Barpanda, Electrochemical Potassium-Ion Intercalation in $Na_xCoO_2$: a novel cathode material for potassium-ion batteries, Chem. Commun. 53 (2017) 8588–8591. https://doi.org/10.1039/C7CC02791E.

[4] C. Vaalma, G. A. Giffin, D. Buchholz, S. Passerini, Non-aqueous K-ion battery based on layered $K_{0.3}MnO_2$ and hard carbon/carbon black, J. Electrochem. Soc. 163 (2016) A1295–A1299. https://doi.org/10.1149/2.0921607jes.

[5] H. Kim, D.-H. Seo, J. C. Kim, S.-H. Bo, L. Liu, T. Shi, G. Ceder, Investigation of potassium storage in layered P3-type $K_{0.5}MnO_2$ cathode, Adv. Mater. 29 (2017) 1702480. https://doi.org/10.1002/adma.201702480.

[6] C. Liu, S. Luo, H. Huang, Z. Wang, A. Hao, Y. Zhai, Z. Wang, $K_{0.67}Ni_{0.17}Co_{0.17}Mn_{0.66}O_2$: a cathode material for potassium-ion battery, Electrochem. Soc. 82 (2017) 150–154. https://doi.org/10.1016/j.elecom.2017.08.008.

[7] X. Wang, X. Xu, C. Niu, J. Meng, M. Huang, X. Liu, Z. Liu, L. Mai, Earth abundant Fe/Mn-based layered oxide interconnected nanowires for advanced K-ion full batteries, Nano Lett. 17 (2017) 544–550. https://doi.org/10.1021/acs.nanolett.6b04611.

[8] N. Naveen, W. B. Park, S. C. Han, S. P. Singh, Y. H. Jung, D. Ahn, K.-S. Sohn, M. Pyo, Reversible $K^+$-insertion/deinsertion and concomitant $Na^+$-redistribution in P′3-$Na_{0.52}CrO_2$ for

high-performance potassium-ion battery cathodes, Chem. Mater. 30 (2018) 2049–2057. https://doi.org/10.1021/acs.chemmater.7b05329.

[9] R.-J. Luo, X.-L. Li, J.-Y. Ding, J. Bao, C. Ma, C.-Y. Du, X.-Y. Cai, X.-J. Wu, Y.-N. Zhou, Suppressing Jahn-Teller distortion and phase transition of $K_{0.5}MnO_2$ by K-site Mg substitution for potassium-ion batteries, Energy Storage Mater. 47 (2022) 408–414. https://doi.org/10.1016/j.ensm.2022.02.027.

[10] N. Recham, G. Rousse, M. T. Sougrati, J.-N. Chotard, C. Frayret, C. S. Mariyappan, B. C. Melot, J.-C. Jumas, J.-M. Tarascon, Preparation and characterization of a stable $FeSO_4F$-based framework for alkali ion insertion electrodes, Chem. Mater. 24 (2012) 4363–4370. https://doi.org/10.1021/cm302428w.

[11] V. Mathew, S. Kim, J. Kang, J. Gim, J. Song, J. P. Baboo, W. Park, D. Ahn, J. Han, L. Gu, Y. Wang, Y.-S. Hu, Y.-K. Sun, J. Kim, Amorphous iron phosphate: potential host for various charge carrier ions, NPG Asia Mater. 6 (2014) e138. https://doi.org/10.1038/am.2014.98.

[12] J. Han, G.-N. Li, F. Liu, M. Wang, Y. Zhang, L. Hu, C. Dai, M. Xu, Investigation of $K_3V_2(PO_4)_3$/C nanocomposites as high-potential cathode materials for potassium-ion batteries, Chem. Commun. 53 (2017) 1805–1808. https://doi.org/10.1039/C6CC10065A.

[13] K. Chihara, A. Katogi, K. Kubota, S. Komaba, $KVPO_4F$ and $KVOPO_4$ toward 4 volt-class potassium-ion batteries, Chem. Commun 53 (2016) 5208–5211. https://doi.org/10.1039/C6CC10280H.

[14] W. B. Park, S. C. Han, C. Park, S. U. Hong, U. Han, S. P. Singh, Y. H. Jung, D. Ahn, K.-S. Sohn, M. Pyo, $KVP_2O_7$ as a robust high-energy cathode for potassium-ion batteries: pinpointed by

a full screening of the inorganic registry under specific search conditions, Adv. Energy Mater. 8 (2018) 1703099. https://doi.org/10.1002/aenm.201703099.

[15] C. D. Wessells, S. V. Peddada, R. A. Huggins, Y. Cui, Nickel hexacyanoferrate nanoparticle electrodes for aqueous sodium and potassium ion batteries, Nano Lett. 11 (2011) 5421–5425. https://doi.org/10.1021/nl203193q.

[16] J. Wang, L. Zhang, L. Yu, Z. Jiao, H. Xie, X. W. (D.) Lou, X. W. Sun, A bi-functional device for self-powered electrochromic window and self-rechargeable transparent battery applications, Nat. Commun. 5 (2014) 4921. https://doi.org/10.1038/ncomms5921.

[17] E. Nossol, V. H.R. Souza, A. J.G. Zarbin, Carbon nanotube/prussian blue thin films as cathodes for flexible, transparent and ITO-free potassium secondary battery, J. Colloid Interface Sci. 478 (2016) 107–116. https://doi.org/10.1016/j.jcis.2016.05.056.

[18] Y.-H. Zhu, Y.-B. Yin, X. Yang, T. Sun, S. Wang, Y.-S. Jiang, J.-M. Yan, X. Zhang, Transformation of rusty stainless-steel meshes into stable, low-cost, and binder-free cathodes for high-performance potassium-ion batteries, Angew. Chem. Int. Ed. 56 (2107) 7881–7885. https://doi.org/10.1002/anie.201702711.

[19] M. J. Piernas-Muñoz, E. Castillo-Martínez, O. Bondarchuk, M. Armand, T. Rojo, Higher voltage plateau cubic prussian white for Na-ion batteries, J. Power Sources. 324 (2016) 766–773. https://doi.org/10.1016/j.jpowsour.2016.05.050.

[20] P. Padigi, J. Thiebes, M. Swan, G. Goncher, D. Evans, R. Solanki, Prussian Green: A high rate capacity cathode for potassium ion batteries, Electrochim. Acta. 166 (2015) 32–39. https://doi.org/10.1016/j.electacta.2015.03.084.

[21] Z. Shadike, D.-R. Shi, T.- Wang, M.-H. Cao, S.-F. Yang, J. Chen, Z.-W. Fu, Long life and high-rate berlin green $FeFe(CN)_6$ cathode material for a non-aqueous potassium-ion battery, J. Mater. Chem. A. 5 (2017) 6393–6398. https://doi.org/10.1039/C7TA00484B.

[22] Y. Chen, W. Luo, M. Carter, L. Zhou, J. Dai, K. Fu, S. Lacey, T. Li, J. Wan, X. Han, Y. Bao, L. Hu, Organic electrode for non-aqueous potassium-ion batteries, Nano Energy. 18 (2015) 205–211. https://doi.org/10.1016/j.nanoen.2015.10.015.

[23] Z. Jian, Y. Liang, I. A. Rodríguez-Pérez, Y. Yao, X. Ji., Poly(anthraquinonyl sulfide) cathode for potassium-ion batteries, Electrochem. Commun. 71 (2016) 5–8. https://doi.org/10.1016/j.elecom.2016.07.011.

[24] N. V. Besprozvannykh, O. Y. Sinel'nikovaa, S. K. Kuchaeva, V. L. Ugolkov, V. I. Al'myashev, A. M. Smirnova, L. A. Koptelova, S. A. Petrov, Sol-gel synthesis and leaching of potassium hollandites, Russ. J. Appl. Chem. 88 (2015) 192–196. https://doi.org/10.1134/S1070427215020020.

[25] M. Sakao, N. Kijima, K. Kataoka, J. Akimoto, T. Okutani, Synthesis and electrochemical properties of hollandite-type $K_xTiO_2$, Key Eng. Mater. 485 (2011) 123–126. https://doi.org/10.4028/www.scientific.net/KEM.485.123.

[26] O. A. Drozhzhin, V. V. Grigoriev, A. M. Alekseeva, S. V. Ryazantsev, O. A. Tyablikov, D. Chernyshov, A. M. Abakumov, E. V. Antipov, Phase transformations and charge ordering during $Li^+$ intercalation into hollandite-type $TiO_2$ studied by *operando* synchrotron X-ray powder diffraction, Eur. J. Inorg. Chem. 9 (2020) 743–748. https://doi.org/10.1002/ejic.201901153.

[27] M. Sakao, N. Kijima, J. Akimoto, T. Okutani, Synthesis, crystal structure, and electrochemical properties of hollandite-type $K_{0.008}TiO_2$, Solid State Ion. 225 (2012) 502–505. https://doi.org/10.1016/j.ssi.2011.11.023.

[28] M. Sakao, N. Kijima, J. Akimoto, T. Okutani, Lithium insertion and extraction properties of hollandite-type $K_xTiO_2$ with different K content in the tunnel Space, Solid State Ion. 243 (2013) 22–29. https://doi.org/10.1016/j.ssi.2013.04.013.

[29] S. Liu, L. Kang, J. Zhang, E. Jung, S. Lee, S. C. Jun, Structural engineering and surface modification of MOF-derived cobalt-based hybrid nanosheets for flexible solid-state supercapacitors, Energy Storage Mater. 32 (2020) 167–177. https://doi.org/10.1016/j.ensm.2020.07.017.

[30] S. Liu, L. Kang, S. C. Jun, Challenges and strategies toward cathode materials for rechargeable potassium-ion batteries, Adv. Mater. 32 (2021) 2004689. https://doi.org/10.1002/adma.202004689.

[31] S. Liu, L. Kang, J. Henzie, J. Zhang, J. Ha, M. A. Amin, M. S. A. Hossain, S. C. Jun, Y. Yamauchi, Recent advances and perspectives of battery-type anode materials for potassium ion storage, ACS Nano 15 (2021) 18931–18973. https://doi.org/10.1021/acsnano.1c08428.

[32] S. Liu, L. Kang, J. Zhang, S. C. Jun, Y. Yamauchi, Carbonaceous anode materials for non-aqueous sodium- and potassium-ion hybrid capacitors, ACS Energy Letters 6 (2021) 4127–4154. https://doi.org/10.1021/acsenergylett.1c01855.

[33] P. E. Blöchl, Projector augmented-wave method, Phys. Rev. B: Condens. Matter Mater. Phys. 50 (1994) 17953–17979. https://doi.org/10.1103/PhysRevB.50.17953.

[34] G. Kresse, J. Furthmuller, Efficient iterative schemes for *ab initio* total-energy calculations using a plane-wave basis set, Phys. Rev. B: Condens. Matter Mater. Phys. 54 (1996) 11169–11186. https://doi.org/10.1103/PhysRevB.54.11169.

[35] J. P. Perdew, K. Burke, M. Ernzerhof, Generalized gradient approximation made simple, Phys. Rev. Lett. 77 (1996) 3865–3868. https://doi.org/10.1103/PhysRevLett.77.3865.

[36] K. Okhotnikov, T. Charpentier, S. Cadars, Supercell program: a combinatorial structure-generation approach for the local-level modeling of atomic substitutions and partial occupancies in crystals, J. cheminform. 8 (2016) 17. https://doi.org/10.1186/s13321-016-0129-3.

[37] K. Momma, F. Izumi, *VESTA 3* for three-dimensional visualization of crystal, volumetric and morphology data, J. Appl. Crystallogr. 44 (2011) 1272–1276. https://doi.org/10.1107/S0021889811038970.

[38] Y. Koyama, H. Arai, I. Tanaka, Y. Uchimoto, Z. Ogumi, Defect chemistry in layered $LiMO_2$ (M= Co, Ni, Mn, and $Li_{1/3}Mn_{2/3}$) by first-principles calculations, Chem. Mater. 24 (2012) 3886–3894. https://doi.org/10.1021/cm3018314.

[39] S.-H. Choe, C. J.-Yu, K.-C. Ri, J.-S. Kim, U.-G. Jong, Y.-H. Kye, S.-N. Hong, First-principles study of $Na_xTiO_2$ with trigonal bipyramid structures: an insight into sodium-ion battery anode applications, Phys. Chem. Chem. Phys. 16 (2019) 8408–8417. https://doi.org/10.1039/C9CP00267G.

[40] S. Zhao Z. Liu G. Xie, Z. Guo, S. Wang, J. Zhou, X. Xie, B. Sun, S. Guo, G. Wang, High-efficiency cathode potassium compensation and interfacial stability improvement enabled by dipotassium squarate for potassium-ion batteries. Energy Environ. Sci. 15 (2022) 3015–3023. https://doi.org/10.1039/D2EE00833E.

[41] T. Sasaki, M. Watanabe, Y. Fujiki, Structure of $K_{1.0}Ti_8O_{16}$ and $K_{0.0}Ti_8O_{16}$. Acta Cryst. B49 (1993) 838–841. https://doi.org/10.1107/S0108768193004677.

[42] J. Zou, S. Chen, Z. Wu, J. Gao, P. Chen, Q. Ran, S. Li, L. Wang, X. Niu, Understanding the electrochemical properties and phase transformations of layered $VOPO_4 \cdot H_2O$ as a potassium-ion battery cathode. J. Power Sources. 480 (2020) 228864. https://doi.org/10.1016/j.jpowsour.2020.228864.

[43] J. C. Pérez-Flores, C. Baehtz, A. Kuhn, F. García-Alvarado, Hollandite-type $TiO_2$: a new negative electrode material for sodium-ion batteries, J. Mater. Chem. A 2 (2014) 1825–1833. https://doi.org/10.1039/C3TA13394J.

[44] A. Duarte, P. Díaz-Carrasco, A. Kuhn, A. Basa, F. García-Alvarado, Deepening into the charge storage mechanisms and electrochemical performance of $TiO_2$ hollandite for sodium-ion batteries, Electrochim. Acta, In Press (2022) 140872.

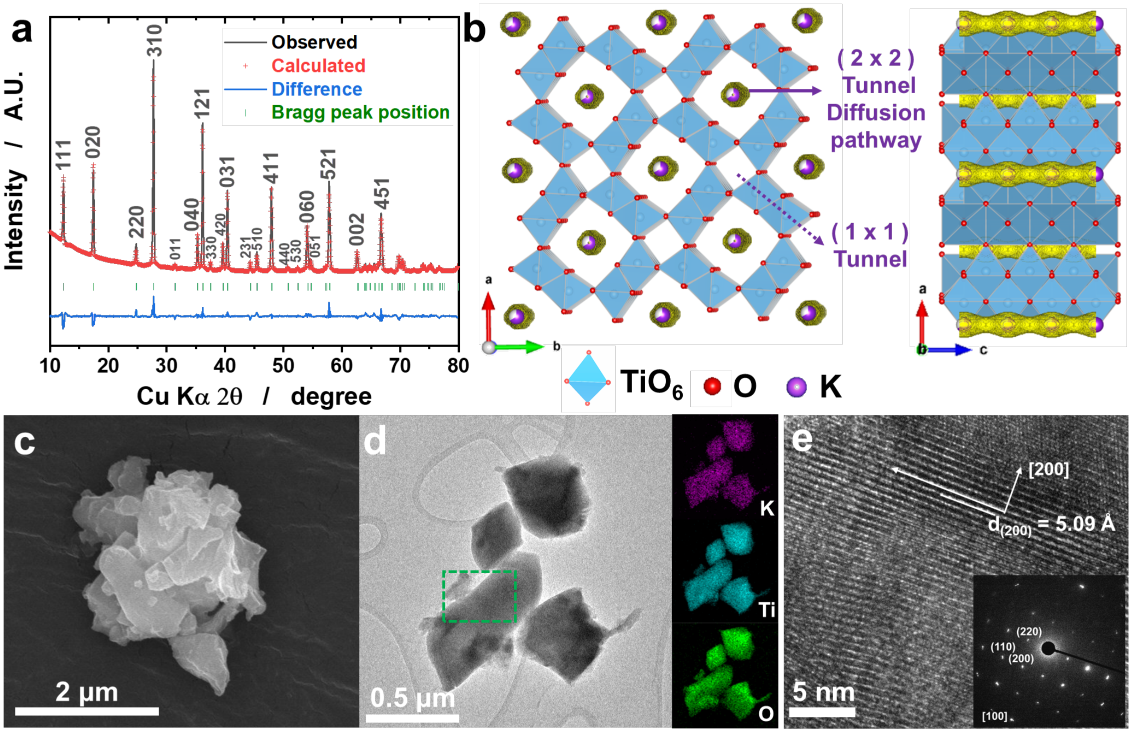


**Fig. 1**. (a) Rietveld refinement of XRD pattern of $K_{0.17}TiO_2$. (b) BVS energy map in tetragonal *I*4/m model structure of $K_{0.17}TiO_2$ for ab plane and ac plane. (c) SEM image and (d) TEM bright-field image with EDS mapping images of $K_{0.17}TiO_2$ particle. (e) HR-TEM image and corresponding SAED pattern of $K_{0.17}TiO_2$.

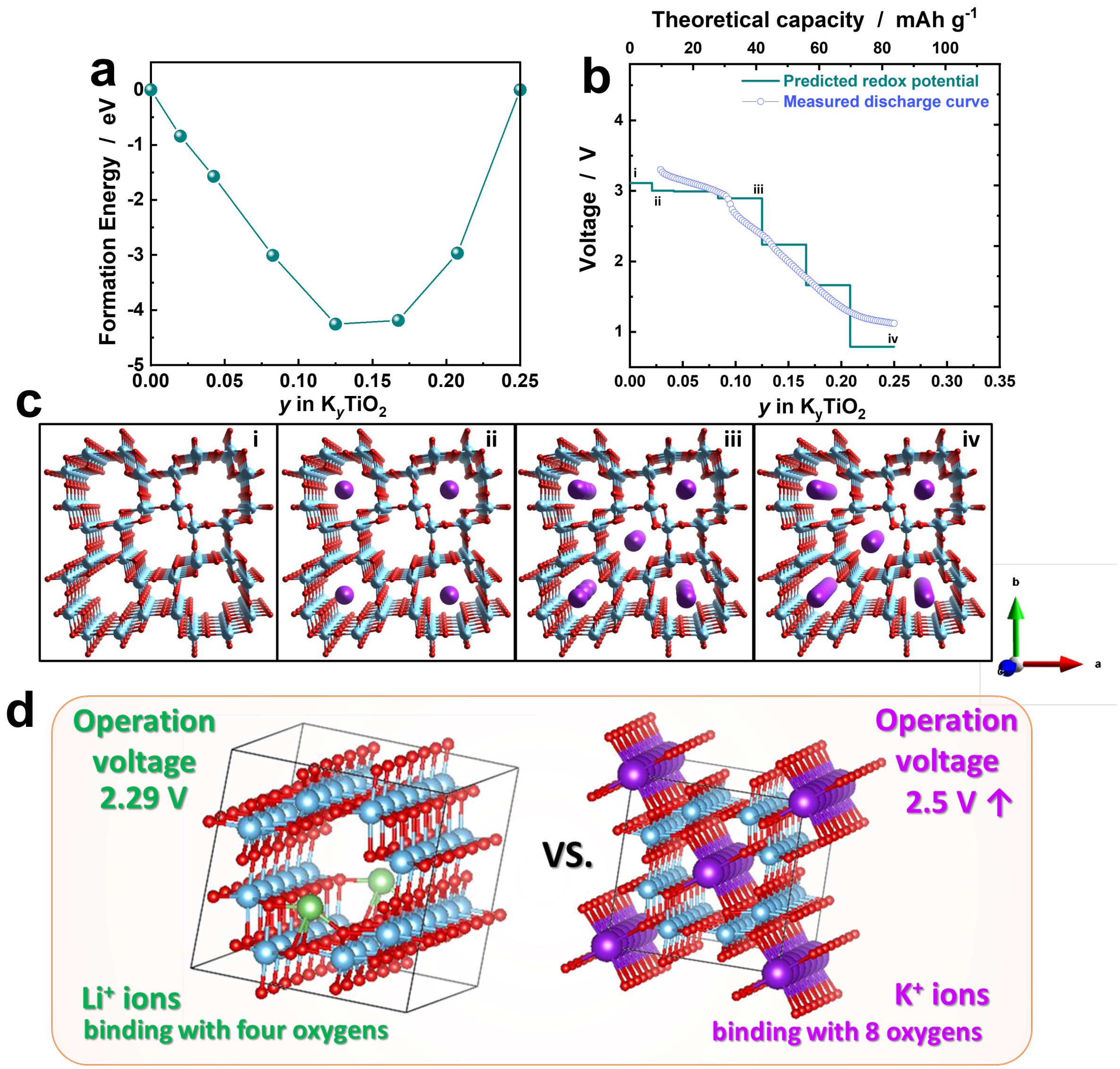


**Fig. 2**. (a) Calculated formation energy versus the fractional K concentration in the K-$TiO_2$ (H) compound, (b) redox potential compared with measured OCV curve, and (c) selected atomistic structures from low to high K concentrations. K, Ti, and O are shown in purple, blue, and red, respectively. (d) Schematic illustration summarizing high operation voltage of $K_{0.17}TiO_2$. K, Li, Ti, and O are shown in purple, green, blue, and red, respectively.

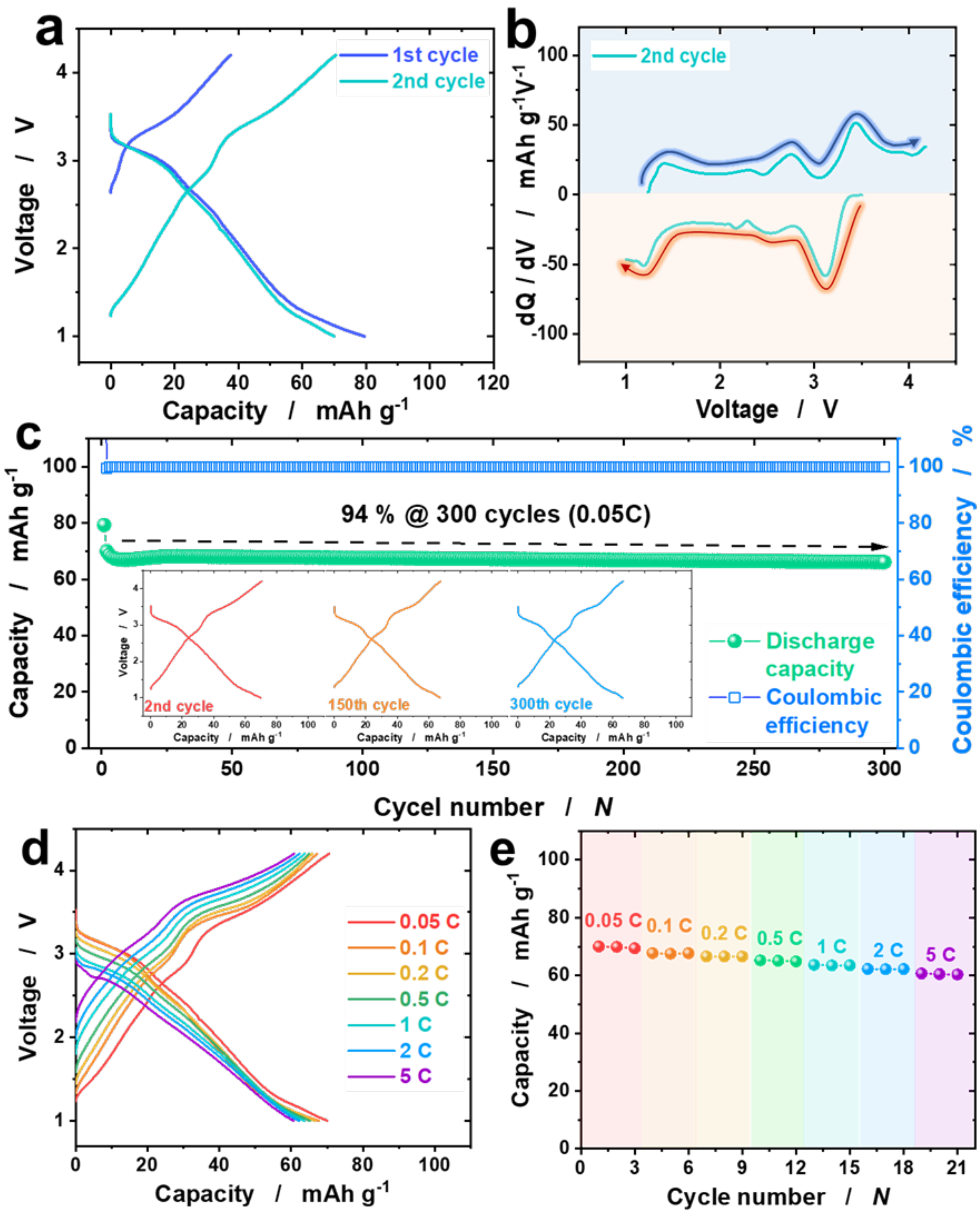


**Fig. 3.** (a) First charge–discharge curve of $K_{0.17}TiO_2$. (b) dQ/dV plot of $K_{0.17}TiO_2$ at first cycle. (c) Cycle performance of $K_{0.17}TiO_2$ at 0.05C (inset: voltage curves at each cycle). (d) Voltage curves at each rate and (e) corresponding rate capability of $K_{0.17}TiO_2$.

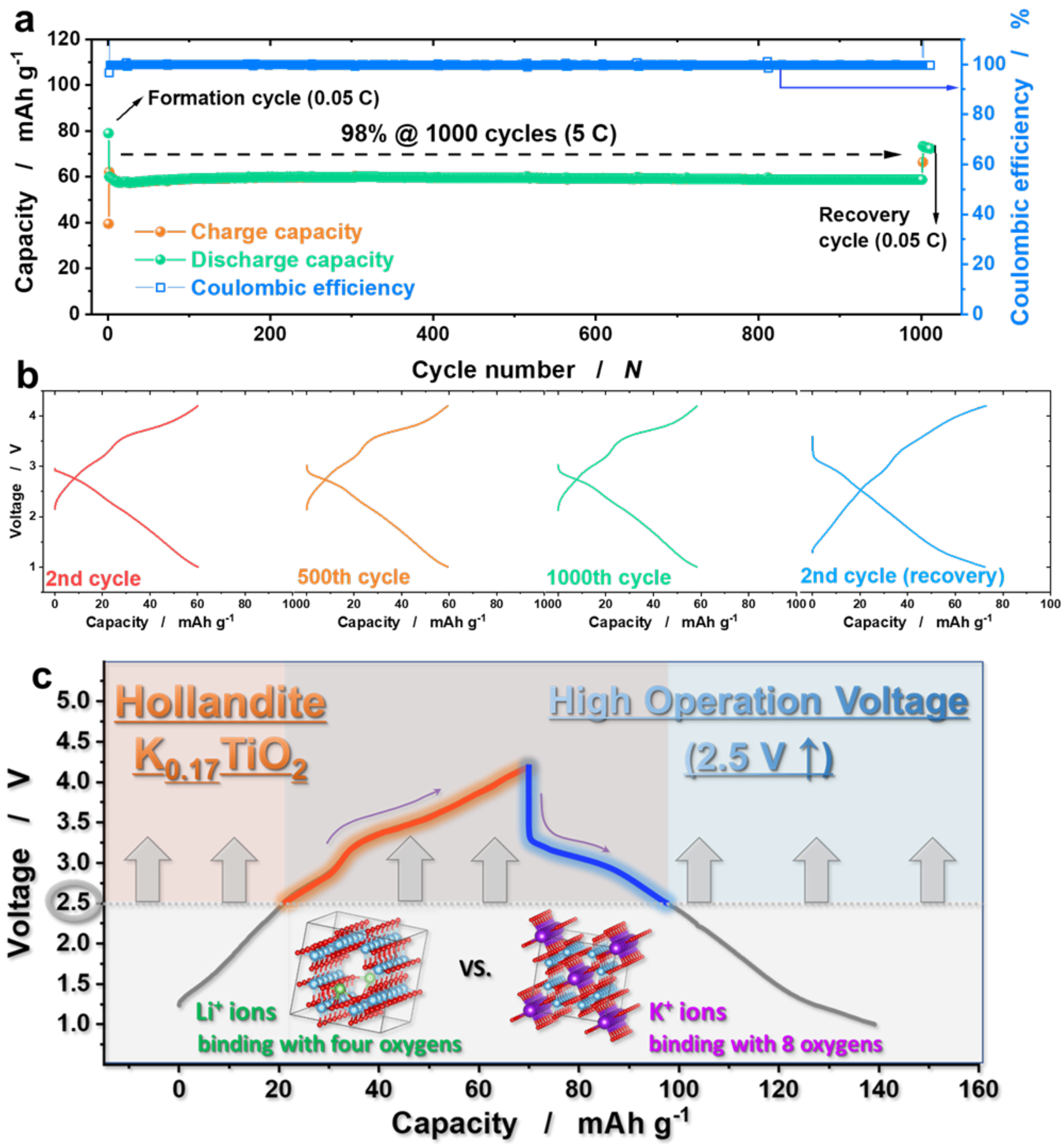


**Fig. 4**. (a) Long-term high-rate cycle performance for 1000 cycles at 5C and corresponding voltage curves at each cycle of $K_{0.17}TiO_2$. (c) Schematic illustration depicting high operation voltage of $K_{0.17}TiO_2$.

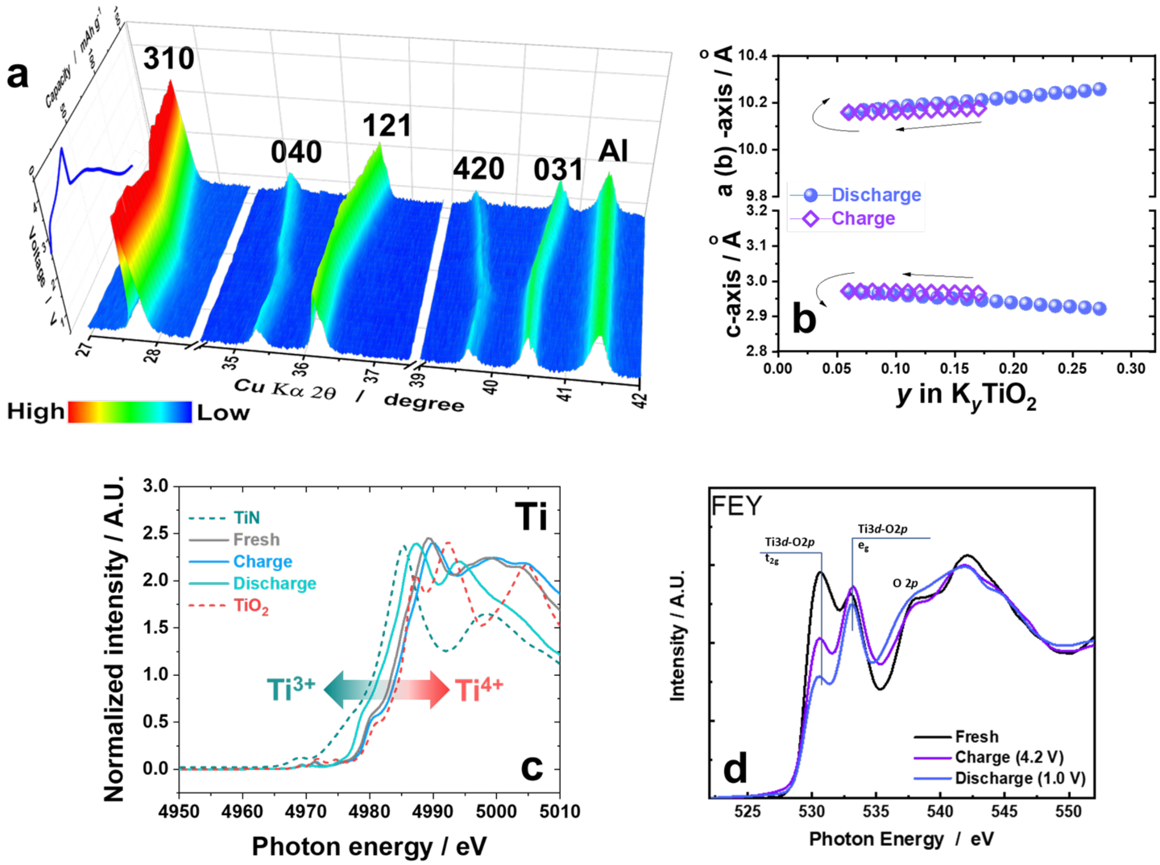


**Fig. 5.** *Operando* XRD result of $K_{0.17}TiO_2$ during initial charge/discharge. (b) Corresponding lattice parameters calculated from the operando XRD result of $K_{0.17}TiO_2$. (c) XANES Ti K-edge spectra of $K_{0.17}TiO_2$. (d) XANES O K-edge spectra of $K_{0.17}TiO_2$.

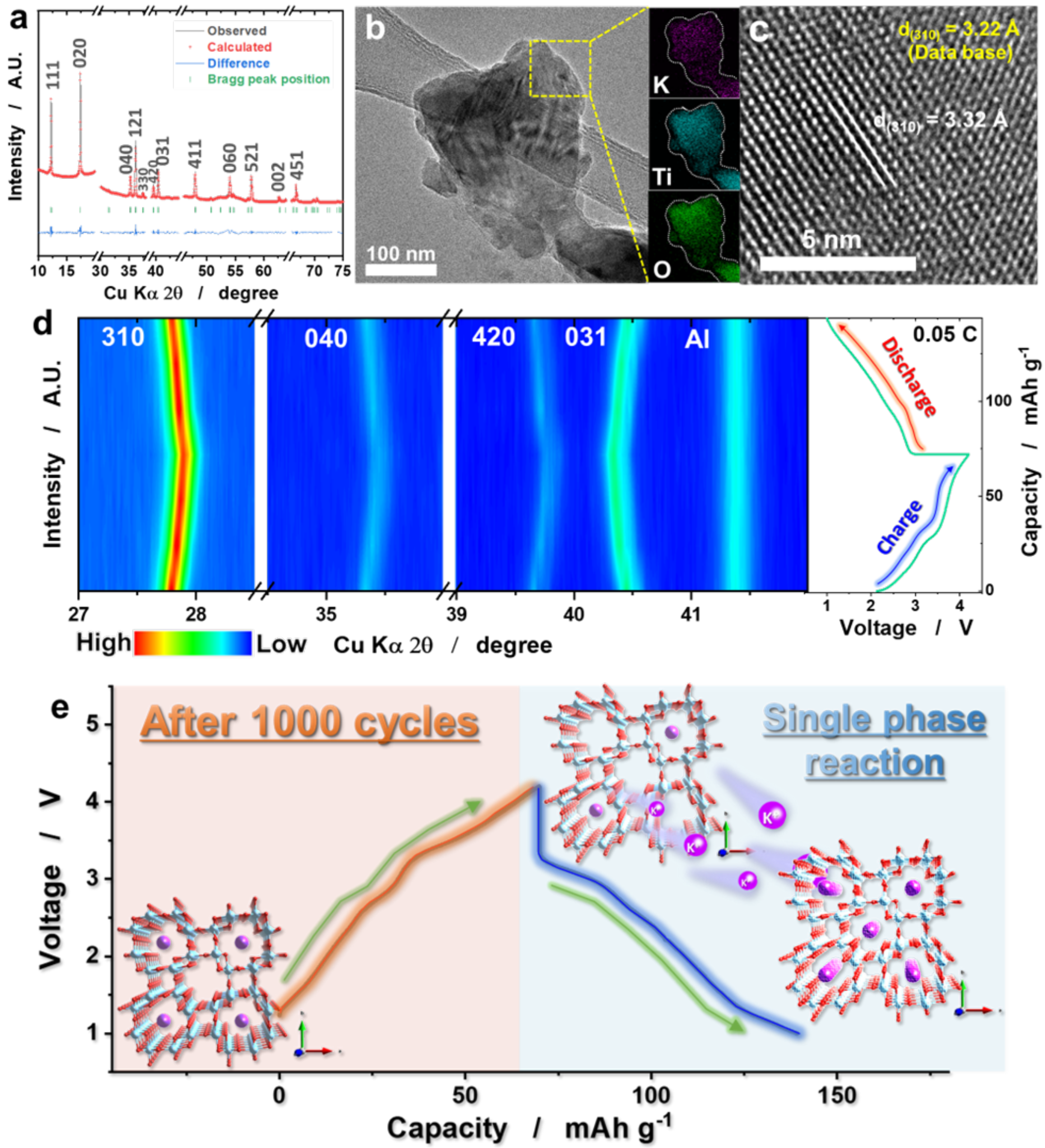


**Fig. 6**. (a) Rietveld refinement of XRD data, (b) TEM bright-field image with EDS mapping images, (c) HR-TEM image, and (d) *o*-XRD result of $K_{0.17}TiO_2$ after 1000 cycles. (e) Schematic illustration summarizing cycle stability of $K_{0.17}TiO_2$.

**Table 1**. Comparison of electrochemical performances of tunnel type $K_yTiO_2$ with different type of charge carrier.

| *Materials* | *Voltage range (V)* | *Charge carrier* | *Specific capacity (mAh g$^{-1}$) / Current (mA g$^{-1}$)* | *Capacity retention (%) / cycles* | *Energy density* | *Ref.* |
|---|---|---|---|---|---|---|
| **$K_{0.17}TiO_2$** | **2.0 – 4.2** | **$K^+$** | **79 / 15.5** | **94 / 300 (from 2$^{nd}$ cycle)**<br>**84 / 300 (from 1$^{st}$ cycle)** | **176** | **This work** |
| **$K_{0.17}TiO_2$** | **2.0 – 4.2** | **$K^+$** | **58.7 / 1550** | **98 / 1000** | **161** | **This work** |
| $K_{0.08}TiO_2$ | 1.0 – 4.8 | $Li^+$ | 92 / 10 | 56 / 50 | 153 | 25 |
| $K_{0.13}TiO_2$ | 1.0 – 3.0 | $Li^+$ | 63 / 10 | 44 / 50 | 100 | 28 |
| $K_{0.095}TiO_2$ | 1.0 – 3.0 | $Li^+$ | 88 / 10 | 34 / 50 | 140 | 28 |
| $TiO_2$ (Hollandite) | 0.2 – 2.7 | $Na^+$ | 110 / 5 (2$^{nd}$ cycle) | 72 / 10 (from 2$^{nd}$ cycle) | 74 (2$^{nd}$ cycle) | 43 |
| $TiO_2$ (Hollandite) | 0.01 – 3.0 | $Na^+$ | 117 / 42 (2$^{nd}$ cycle) | 89 / 300 (from 2$^{nd}$ cycle) | 172 | 44 |